Xia, Q, Robertson, N, Heymans, C, Amon, A, Asgari, M, Cai, Y-C, Erben, T, Harnois-Déraps, J, Hildebrandt, H, Kannawadi, A, Kuijken, K, Schneider, P, Sifón, C, Tröster, T and Wright, AH

 A gravitational lensing detection of filamentary structures connecting luminous red galaxies

http://researchonline.ljmu.ac.uk/id/eprint/13333/

Article

For more information please contact researchonline@ljmu.ac.uk

Astronomy & Astrophysics

A gravitational lensing detection of filamentary structures connecting luminous red galaxies

Qianli Xia[1], Naomi Robertson[2], Catherine Heymans[1,3], Alexandra Amon[1,4], Marika Asgari[1], Yan-Chuan Cai[1],
Thomas Erben[5], Joachim Harnois-Déraps[1], Hendrik Hildebrandt[3], Arun Kannawadi[6], Konrad Kuijken[6],
Peter Schneider[5], Cristóbal Sifón[7], Tilman Tröster[1], and Angus H. Wright[3]

[1] Institute for Astronomy, University of Edinburgh, Royal Observatory, Blackford Hill, Edinburgh EH9 3HJ, UK
   e-mail: qx211@roe.ac.uk
[2] Department of Astrophysics, University of Oxford, Keble Road, Oxford OX1 3RH, UK
   e-mail: naomi.robertson@physics.ox.ac.uk
[3] German Centre for Cosmological Lensing, Astronomisches Institut, Ruhr-Universität Bochum, Universitätsstr, Bochum, Germany
[4] Kavli Institute for Particle Astrophysics & Cosmology, Stanford University, PO Box 2450, Stanford, CA 94305, USA
[5] Argelander-Institut für Astronomie, Universitï Bonn, Auf dem Hügel 71, 53121 Bonn, Germany
[6] Leiden Observatory, Leiden University, PO Box 9513, 2300 Leiden, The Netherlands
[7] Instituto de Física, Pontificia Universidad Católica de Valparaíso, Casilla 4059, Valparaíso, Chile

ABSTRACT

We present a weak lensing detection of filamentary structures in the cosmic web, combining data from the Kilo-Degree Survey, the Red Cluster Sequence Lensing Survey, and the Canada-France-Hawaii Telescope Lensing Survey. The line connecting luminous red galaxies with a separation of $3-5\,h^{-1}$ Mpc was chosen as a proxy for the location of filaments. We measured the average weak lensing shear around $\sim$11 000 candidate filaments selected in this way from the Sloan Digital Sky Survey. After nulling the shear induced by the dark matter haloes around each galaxy, we reported a 3.4σ detection of an anisotropic shear signal from the matter that connects them. Adopting a filament density profile, motivated from N-body simulations, the average density at the centre of these filamentary structures was found to be 15 ± 4 times the critical density.

1. Introduction

Galaxy surveys, including the 2dF Galaxy Redshift Survey (Colless et al. 2001) and the Sloan Digital Sky Survey (SDSS; Zehavi et al. 2011), have shown that visible matter in our Universe is not uniformly distributed on intermediate scales $\sim$100 h^{-1} Mpc. Instead, a web-like structure is observed with clusters of galaxies identifying the densest regions. N-body simulations predict the existence of these large-scale structures (e.g. Bond et al. 1996; Springel et al. 2005), suggesting a hierarchical structure formation for the cosmic web. We can classify the web (e.g. Eardley et al. 2015) into regions of clusters, filaments, sheets and voids. In this cosmic web, large under-dense regions (voids) are enclosed by anisotropically collapsed surface structures (sheets) and line structures (filaments) which intersect at the most over-dense isotropic regions (clusters). The Zel'dovich approximation predicts that $\sim$42% of the mass of the Universe is in a filament environment (Zel'dovich 1970), and this has been confirmed by simulations (Aragón-Calvo et al. 2010). However, as filament environments do not display a very high density contrast, this makes direct observations challenging.

One way to observe filaments is from the X-ray emission induced by the warm hot intergalactic medium (WHIM) with several inter-cluster filaments investigated in this way (Briel & Henry 1995; Kull & Böhringer 1999; Werner et al. 2008). There are also reported detections of filaments using over-densities of galaxies (Pimbblet & Drinkwater 2004; Ebeling et al.

2004). Recently, two independent studies (de Graaff et al. 2019; Tanimura et al. 2019) detected the Sunyaev–Zel'dovich (SZ) signal from the ionised gas in the cosmic web. They estimated the density of ionised gas to be $\sim$(28 ± 12)% of the total baryon density in the Universe, close to resolving the missing baryon problem (Bregman 2007).

In this paper, we investigate the use of weak gravitational lensing to detect filaments. Based on the distortion of light rays around massive objects, gravitational lensing probes the total mass traced by the large-scale structures and is, therefore, highly complementary to the SZ detection of the gas. Although Dietrich et al. (2012) made a direct weak lensing detection of a filament connecting two massive Abell clusters, the direct detection of typical individual filaments is limited by the low signal-to-noise measurement, and most studies stack large samples of candidate filaments and analyse the resulting average weak lensing signal instead (Mead et al. 2010; Clampitt et al. 2016; Epps & Hudson 2017; Kondo et al. 2019).

Clampitt et al. (2016; hereafter C16) determined the weak lensing signal at around 135 000 pairs of SDSS Luminous Red Galaxies (LRGs) with a projected separation $6\,h^{-1}$ Mpc $\leq R_{\rm sep} \leq 14\,h^{-1}$ Mpc and a redshift separation of $\Delta z < 0.004$. Using a "nulling" estimator that cancels the spherically symmetric contribution of the LRG haloes in the shear measurement, they reported a 4.5σ detection of the filament lensing signal. In another study, Epps & Hudson (2017) used $\sim$23 000

pairs of LRGs from the Baryon Oscillation Spectroscopic Survey (BOSS) LOWZ and CMASS samples as tracers of filaments. Using data from the Canada-France-Hawaii Telescope Lensing Survey (CFHTLenS), they performed a mass reconstruction of a set of stacked LRG pairs with a projected angular separation between 6 and $10 \, h^{-1}$ Mpc and a redshift separation $\Delta z < 0.003$. After subtracting the signal from a mass reconstruction of a set of stacked LRG pairs with the same separation on the sky but a greater redshift separation ($0.033 < \Delta z < 0.04$) such that haloes should not be physically connected, they reported a 5σ detection of a filament lensing signal. A more recent study (Kondo et al. 2019) used 70 210 pairs of LRGs from the CMASS sample with a projected separation between 6 and $14 \, h^{-1}$ Mpc and a line-of-sight separation of less than $6 \, h^{-1}$ Mpc. Using the Subaru Hyper Suprime-Cam (HSC) first-year galaxy shape catalogue and adopting the C16 nulling approach they reported 3.9σ detection of a filament signal.

We note that the methodology taken in these previous studies can be understood as a three-point galaxy–galaxy-shear correlation function conditioned on specific intervals of separation between lens galaxies (Schneider & Watts 2005). The full suite of the galaxy-galaxy-galaxy lensing (GGGL) statistics have been applied to the Red-Sequence Cluster Survey (Simon et al. 2008) and CFHTLenS (Simon et al. 2019) to measure the excess mass around galaxy pairs separated by $\lesssim 300 \, h^{-1}$ kpc.

In this paper, we present the weak lensing signal measured between 11 706 LOWZ LRG pairs that have a separation of $3-5 \, h^{-1}$ Mpc, combining three public weak lensing surveys; the KiDS+VIKING-450 survey (KV450; Hildebrandt et al. 2018; Wright et al. 2019), the Red Cluster Sequence Lensing Survey (RCSLenS; Hildebrandt et al. 2016), and the CFHTLenS (Heymans et al. 2012). We improve the nulling methodology described in C16 to deal with contamination from filament tracers and use a large suite of N-body simulations to validate our pipeline and compare our results. A standard ΛCDM cosmology has been adopted throughout this study to calculate distances with a matter density $\Omega_{\rm m} = 0.3$, energy density $\Omega_{\Lambda} = 0.7$, effective number of neutrino species $N_{\rm eff} = 3.04$, baryon density $\Omega_{\rm b} = 0.0$ and current Hubble constant $H_0 = 100 \, h \, {\rm km \, s^{-1} \, Mpc^{-1}}$ where h is the Hubble parameter $h = 0.7$.

This paper is structured as follows. In Sect. 2, we describe the survey data and simulations. Section 3 summarises the weak lensing formalism, the adopted filament model, and methodology. We show our results in Sect. 4 and conclude in Sect. 5. In Appendix A, we present a validation of our nulling technique. In Appendix B, we document the spherical rotation methodology that is required for high declination surveys.

2. Surveys and simulations

2.1. The lensing surveys

The properties of the three lensing surveys, KV450, RCSLenS, and CFHTLenS, are listed in Table 1. They share a similar data processing pipeline, where the shape measurement of galaxies was conducted using the *lens*fit model fitting code (Miller et al. 2013). This approach convolves the pixelised model Point-Spread-Function with an analytical surface brightness model consisting of bulge and disk components. It uses model fitting to estimate galaxy ellipticites $\epsilon_1^{\rm obs}$ and $\epsilon_2^{\rm obs}$ with an associated inverse variance weight, $w_{\rm s}$. The (reduced) shear (cf. Eq. (4)) is then given by the weighted average of ellipticities, $\gamma_i^{\rm obs} \approx \sum_s w_s \epsilon_i^{\rm obs} / \sum_s w_s$ ($i = 1, 2$). The observed shear is biased with respect to the true shear and is typically described by the linear

bias model (Heymans et al. 2006) as

$$\gamma^{\rm obs} = (1 + m)\gamma^{\rm true} + c, \tag{1}$$

In all of these three surveys, the shear multiplicative bias terms were characterised as a function of the signal-to-noise ratio and size of the galaxies, thereby allowing us to calculate the bias for an arbitrary selection of galaxies. The correction for this multiplicative bias was carried out as it was in Velander et al. (2014).

Photometric redshifts, z_B, were estimated using the Bayesian photometric redshift algorithm (BPZ; Benítez 2000) as detailed in Hildebrandt et al. (2012). Wright et al. (2019) and Hildebrandt et al. (2018) show how the photometric redshifts distributions for KV450 are then calibrated using the "weighted direct calibration" method, with weights estimated using a deep spectroscopic training sample in 9-band $ugriZYJHK_s$ magnitude space. No such calibration was performed for the 4-band (RCSLenS) or 5-band (CFHTLenS) surveys, and instead a probability distribution of true redshifts was estimated from the sum of the BPZ redshift probability distributions. This approach has been demonstrated to carry more systematic error (Choi et al. 2016; Hildebrandt et al. 2017). We discuss how we take this redshift uncertainty into account in our final analysis in Sect. 3.4.

2.2. The BOSS survey

We used the Baryon Oscillation Spectroscopic Survey (BOSS) galaxies from the 12th SDSS Data Release (Alam et al. 2015) to define candidate filaments. Among all three lensing surveys RCSLenS has the most SDSS overlap with almost double that of KV450 or CFHTLenS. Once a robust photometric redshift selection has been applied, however, RCSLenS has only 20%/30% the lensing source density in comparison to CFHTLenS/KV450, (see Table 1 for details).

Given the depth of the lensing surveys and the uncertainty in the high redshift tail of the redshift distribution for CFHTLenS and RCSLenS, we chose to limit our analysis to the LOWZ sample, selected based on colour and magnitude, using a redshift cut $0.15 < z < 0.43$ (Ross et al. 2012). We did not consider the higher redshift CMASS sample. The typical virial halo mass of LOWZ galaxies is $\sim 5.2 \times 10^{13} \, h^{-1} \, M_{\odot}$ (Parejko et al. 2013). These haloes have a typical virial radius $\sim 1 \, h^{-1}$ Mpc.

2.3. Simulations

We used the Scinet Light Cone Simulations (SLICS[1]; Harnois-Déraps & van Waerbeke 2015; Harnois-Déraps et al. 2018) to test our methodology. This suite provided us with 819 independent light cones on a $10 \times 10 \, {\rm deg}^2$ patch of the sky. Each light cone was constructed from the full non-linear evolution of 1536^3 particles with $m_{\rm p} = 2.88 \times 10^9 \, h^{-1} \, M_{\odot}$, within a $505^3 (h^{-1} \, {\rm Mpc})^3$ cube. Particles were then projected onto mass sheets at 18 redshifts between $0 < z < 3$, and subsequently inspected to identify dark matter haloes. For each simulation, $100 \, {\rm deg}^2$ light cone mass sheets and haloes were extracted; the former were then ray-traced into lensing shear maps, while the latter were used to generate mock LOWZ galaxies with a halo occupation distribution, optimised so that the clustering of mock galaxies would be consistent with the LOWZ data (see Harnois-Déraps et al. 2018 for details). We find the mock sample variance to be in good agreement with the Jack-knife errors measured directly from the data. Source galaxy positions were

---

[1] http://slics.roe.ac.uk

Table 1. Properties of each of the three lensing surveys used in this analysis.

	KV450	RCSLenS	CFHTLenS
Total area (deg^2)	454	785	154
Unmasked area (deg^2)	341.3	571.7	146.5
Total LOWZ overlap area (deg^2)	135.91	224.63	113.83
z_B selection	$0.1 < z_B < 1.2$	$0.4 < z_B < 1.1$	$0.2 < z_B < 1.3$
n_{eff} (arcmin^{-2})	6.93	2.2	11
Photometric bands	$(u, g, r, i, Z, Y, J, H, K_s)$	(g, r, i, z)	(u^*, g', r', i', z')

Notes. The table lists: the total and effective unmasked survey area, the total LOWZ overlap area, photometric redshift, z_B, selection and the effective number density of lensing sources n_{eff} under the corresponding z_B selection. For the z_B selection, we followed Hildebrandt et al. (2017), Hildebrandt et al. (2016), and Heymans et al. (2012), respectively.

drawn at random, with the shear assigned for a range of redshifts and high number density. We next randomly drew from the SLICS mock source galaxy sample so as to match the corresponding number density and redshift distribution of each of the three surveys, KV450, RCSLenS, and CFHTLenS. Intrinsic galaxy shapes were chosen to match the KiDS ellipticity dispersion (Hildebrandt et al. 2017), which is good description of the ellipticity dispersion that is also found in RCSLenS and CFHTLenS.

3. Summary of weak lensing formalism and methodology

In this section, we summarise the weak gravitational lensing theory following the more detailed derivations in Bartelmann & Schneider (2001). Assuming the thin lens approximation, a foreground object at a position $\boldsymbol{\theta}$ has a 2D comoving surface mass density $\Sigma(\boldsymbol{\theta})$. The convergence is then defined as

$$\kappa(\boldsymbol{\theta}) = \frac{\Sigma(\boldsymbol{\theta})}{\Sigma_{crit}}, \tag{2}$$

where Σ_{crit} is the comoving critical surface density in a flat Universe given by

$$\Sigma_{crit} = \frac{c^2}{4\pi G} \frac{\chi(z_s)}{[\chi(z_s) - \chi(z_l)]\chi(z_l)(1 + z_l)}. \tag{3}$$

Here χ is the comoving distance and z_l, z_s are the redshifts of the lens and source, respectively. Since we are interested in the large scale comoving surface density around filaments, this is the appropriate choice for Σ_{crit} (see Dvornik et al. 2018, for a discussion on the different definitions of Σ_{crit}).

The deflection potential, $\psi(\boldsymbol{\theta})$, is connected to the convergence, κ, via Poisson's equation $\nabla^2 \psi = 2\kappa$, and the complex shear is related to the second derivatives of the deflection potential via

$$\gamma = \gamma_1 + i\gamma_2 = \frac{1}{2}\left(\frac{\partial^2 \psi}{\partial x_1^2} - \frac{\partial^2 \psi}{\partial x_2^2}\right) + i\frac{\partial^2 \psi}{\partial x_1 \partial x_2}, \tag{4}$$

where x_1, x_2 are the horizontal and vertical displacements on the projected sky.

For a filament aligned with the x_1 axis if we assume the deflection potential ψ and convergence κ are both invariant along the filament, then Eq. (4) immediately implies that partial derivatives with respect to the x_1-axis will be equal to zero. This leads to the approximation that for filaments, we should expect to measure $\gamma_1 \approx -\kappa$ and $\gamma_2 \approx 0$. Motivated by the simulation results of Colberg et al. (2005) and Mead et al. (2010) considered the power law density profile around filaments and suggested the

model for the convergence at a distance r from filament centre, measured perpendicular to the major filament axis (x_1-axis)

$$\kappa(r) \approx \frac{\kappa_c}{1 + \left(\frac{r}{r_c}\right)^2}. \tag{5}$$

Here κ_c is the amplitude of the convergence at the filament centre ($r = 0$) and r_c is the half-maximum radius of the density profile.

3.1. Filament candidiate

Colberg et al. (2005) showed that cluster pairs separated by $<5\,h^{-1}$ Mpc are always connected by filamentary structures. We therefore select luminous red galaxy (LRG) pairs in the LOWZ catalogue with redshift separation $\delta z < 0.002$ and a projected separation $3\,h^{-1}$ Mpc $\leq R_{sep} \leq 5\,h^{-1}$ Mpc as our candidate filaments[2] which we will refer to as our physical pairs (PP). Non-physical pairs (NP) are defined to have the same projected separation range but with large line-of-sight separations with $0.033 < \delta z < 0.04$ (corresponding to $\sim 100\,h^{-1}$ Mpc). With such a large physical separation we would not expect to detect a filament signal. The NP therefore provide an important null-test for our methodology.

Our candidates differ from the selection made by C16, Epps & Hudson (2017), de Graaff et al. (2019), Tanimura et al. (2019), and Kondo et al. (2019), who focused on separations of $6-10\,h^{-1}$ Mpc. Our choice maximises signal-to-noise, as shown in our analysis of numerical simulations in Sect. 4.1, but for completeness we also present an analysis of $6-10\,h^{-1}$ Mpc filaments in Sect. 5.

3.2. Stacking method

For each lens filament candidate at redshift $z_l = z_f = (z_{lens\,1} + z_{lens\,2})/2$, we measure the Σ_{crit}-weighted shear, E_f, on a grid (i, j) centred and oriented with the pair of LRGs, where

$$E_f(i, j) = \sum_s w_s \overline{\Sigma_{crit}^{-1}}(z_l) \widetilde{\epsilon}_s^{obs} \Theta_s(i, j), \tag{6}$$

and the sum is taken over all sources[3], s, with $z_B > z_l + 0.1$ and

$$\Theta_s(i, j) = \begin{cases} 1 & \text{if source, } s, \text{ lies in pixel } (i, j), \\ 0 & \text{otherwise.} \end{cases} \tag{7}$$

---

[2] The average 3D separation between these filament candidates is about $7\,h^{-1}$ Mpc.

[3] We use a redshift cut $z_B - z_l > 0.1$ everywhere to ensure that the majority of our source galaxies are behind the foreground galaxies, and not associated with them. Fig. D3 in Amon et al. (2018) demonstrates that with this selection, contamination of the KiDS source sample is negligible for the scales we probe at $>0.1\,h^{-1}$ Mpc.

The complex ellipticity $\widetilde{\epsilon}_s^{obs} = \widetilde{\epsilon}_1^{obs} + i\widetilde{\epsilon}_2^{obs}$ is the observed ellipticity of the source rotated into the reference frame where the filament lies along the x_1 axis. The Σ_{crit} weight converts from a shear estimate to an estimate of the surface mass density Σ in Eq. (2). The grid (i, j) has an extent $[-2R_{sep}, 2R_{sep}] \times [-2R_{sep}, 2R_{sep}]$ and 129^2 pixels, and the pair of lens galaxies that define the filament candidate are positioned to lie at the centre of the pixels at $(-0.5R_{sep}, 0)$ and $(0.5R_{sep}, 0)$.

We also construct a corresponding weight map for each filament candidate,

$$W_f(i, j) = \sum_s w_s \left[\overline{\Sigma_{crit}^{-1}}(z_l) \right]^2 \Theta_s(i, j), \tag{8}$$

where the extra factor of $\overline{\Sigma_{crit}^{-1}}(z_l)$ provides optimal signal-to-noise weighting (Velander et al. 2011).

When rotating each filament pair into a common reference frame, we note that at high declination, the tangent plane method used in Epps & Hudson (2017) and the direct cartesian approximation in C16 results in non-uniform grid cells. As the nulling approach requires a flat geometry on the grid, we found that these approximations lead to a biased result. To solve this problem for high-declination patches, we use the spherical rotation method from de Graaff et al. (2019). This process is detailed in Appendix B, and illustrated in Fig. B.1, with the rotated shear map $(\widetilde{\epsilon}_1, \widetilde{\epsilon}_2)$ defined in Eq. (B.4).

As we have spectroscopic redshifts for the filaments but only photometric redshifts for the sources, the inverse critical surface mass density $\Sigma_{crit}^{-1}(z_l)$ is calculated for each survey as

$$\overline{\Sigma_{crit}^{-1}}(z_l) \equiv \int_{z_l}^{\infty} dz_s\, \overline{p_s}(z_s, z_l) \Sigma_{crit}^{-1}(z_l, z_s) \tag{9}$$

$$= \frac{4\pi G(1 + z_l)\chi(z_l)}{c^2} \int_{z_l}^{\infty} dz_s\, \overline{p_s}(z_s, z_l) \left[1 - \frac{\chi(z_l)}{\chi(z_s)} \right], \tag{10}$$

where $\overline{p_s}$ is the probability distribution of the true redshift of the source galaxies that enter the measurement

$$\overline{p_s}(z_s, z_l) = \frac{\sum\limits_s w_s p_s(z_s|z_B)}{\sum\limits_s w_s}. \tag{11}$$

For CFHTLenS and RCSLenS we use the per-source $p_s(z_s|z_B)$ provided by each survey, even though this has been shown to introduce biases (Choi et al. 2016), which we account for in Sect. 3.4. For KV450 we use the weighted direct calibration method of Hildebrandt et al. (2017) to determine the source redshift distribution $\overline{p_s}(z_s)$ directly for an ensemble of sources. In practice we calculate $\overline{\Sigma_{crit}^{-1}}$ in Eq. (10) at eight z_l values and interpolate to evaluate $\overline{\Sigma_{crit}^{-1}}$ at each filament redshift. The effective $n(z_s)$ for each survey, given by

$$n(z_s) = \int \overline{p_s}(z_s, z_l) p(z_l)\, dz_l, \tag{12}$$

is shown in Fig. 1, with CFHTLenS and KV450 providing a deeper source redshift than RCSLenS.

We correct the measured shear signal E_f, with the signal measured around "random" filaments. This is now a standard procedure in galaxy–galaxy lensing studies (e.g. Mandelbaum et al. 2005) which removes any hidden systematics and reduces sampling variance noise. We create random filament samples for each survey patch, listed in Table 2, by randomly shifting filaments within the same patch while preserving
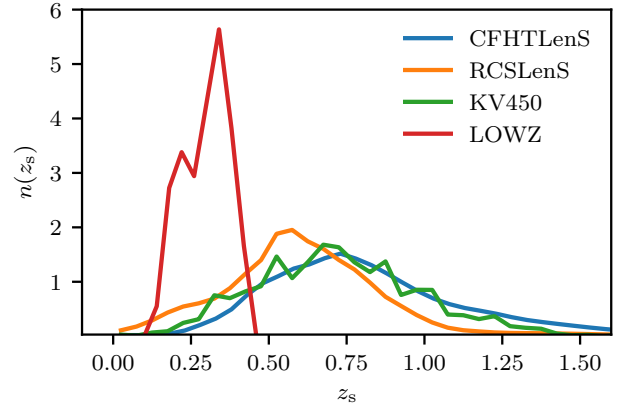
Fig. 1. The effective $n(z)$ of all three lensing surveys, as defined in Eq. (12), when using LOWZ galaxies as lenses. Each curve is normalised such that $\int n(z)\, dz = 1$.

Table 2. Effective area and number of filaments in each survey patch.

Survey	Patch name	A_{eff}^{LOWZ}	$N_{fil},\, 3{\sim}5\, h^{-1}$ Mpc
CFHTLenS	W1$^\triangle$	53.38	1106
	W3$^\triangle$	40.12	835
	W4$^\triangle$	20.34	528
KV450	G9	11.10	305
	G12$^\triangle$	30.08	586
	G15$^\triangle$	94.73	2150
RCSLenS	R0047$^\triangle$	40.27	2111
	R0133	14.25	642
	R1040$^\triangle$	26.94	580
	R1303	4.00	119
	R1514$^\triangle$	32.72	1296
	R1613	9.16	331
	R1645$^\triangle$	22.66	678
	R2143$^\triangle$	42.16	1063
	R2329$^\triangle$	32.09	773
	R2338	0.39	25

Notes. The patches that are used in the analysis are identified with a $\triangle$.

their redshifts, position angles and number density in the patch. As we do not expect any physical signal from the random catalogue, we subtract any measured "random" signal from the data as follows:

$$E_f^{cor} = E_f - \overline{E_{ran}}. \tag{13}$$

Here, for a patch with N_p filament candidates $\overline{E_{ran}}$ is given by

$$\overline{E_{ran}} = \frac{1}{N_R} \frac{1}{N_p} \sum_{r=1}^{N_R} w_{ran} \sum_{k=1}^{N_p} E_r, \tag{14}$$

and

$$w_{ran} = \sum_{k=1}^{N_p} w_f W_f / \sum_{k=1}^{N_p} W_r, \tag{15}$$

where E_r and W_r are the weighted shear (Eq. (6)) and weight (Eq. (8)) but measured around a random pair. w_{ran} is the normalisation weight where N_R is the number of realisations which

ensures $N_R \times N_p$ exceeds 100 000 in each patch[4]. This ensures that the random signal has low scatter so that we can take the mean as the random correction.

The random-corrected shear map E_f^{cor} and weight map W_f are then optimally combined over all filament candidates to determine the total weighted shear signal, $\mathcal{T}$, over the full sample,

$$\mathcal{T}(i,j) = \frac{1}{K} \frac{\sum\limits_f w_f E_f^{cor}}{\sum\limits_f w_f W_f} \quad (16)$$

where $w_f = w_{lens\,1} \times w_{lens\,2}$ is the product of the recommended SDSS completeness weights for the LOWZ galaxies to account for any extra galaxy pairs in the case of fibre collision. We have also applied the multiplicative calibration correction at this stage which is given by Velander et al. (2014) as

$$K(i,j) = \frac{\sum\limits_f w_f \sum\limits_s w_s \left[\overline{\Sigma_{crit}^{-1}}(z_f)\right]^2 (1+m_s)\,\Theta_s(i,j)}{\sum\limits_f w_f W_f}. \quad (17)$$

The total weighted shear $\mathcal{T}(i,j)$ is a combination of both the shear contribution from the haloes surrounding the LOWZ LRGs and the contribution from any filament that connects them.

In order to isolate the filament we apply the "nulling" procedure described in Appendix A to get a final measurement of the shear contribution from the filament only, $\mathcal{F}(r)$, as a function of the distance, r, from the central filament axis,

$$\mathcal{F}(r) = \frac{\sum\limits_{i=i_{min}}^{i_{max}} \mathcal{N}[\mathcal{T}(i,r)]}{i_{max} - i_{min} + 1}. \quad (18)$$

Here $\mathcal{N}$ is the nulling operator given in Eq. (A.11) and the summation over pixels from an i_{min} to i_{max} runs along the filament from $-0.438R_{sep}$ to $0.438R_{sep}$. This value was found to minimise any residual contribution from the haloes positioned at $\pm 0.5R_{sep}$, that remains after a nulling analysis of the SLICS simulation (see Sect. 4.1). Our nulling operator $\mathcal{N}$ combines the shear values measured at 8 different positions (including 4 positions from a reflection about the filament axis) which alternatingly rotate around the two haloes. In this way the isotropic contribution from the parent haloes sum to zero (i.e. "null") and any anisotropic contribution in-between the two haloes can be recovered. In Appendix A, we provide a detailed proof and compare our nulling approach to that adopted in C16. Through tests on a fiducial model, we show that the C16 nulling approach produces a biased result on large scales.

In this derivation we have carried both components of the shear with $\mathcal{F} = \mathcal{F}_{\gamma_1} + i\mathcal{F}_{\gamma_2}$. Given the Mead et al. (2010) filament model, where $\kappa = -\gamma_1$, we expect $\mathcal{F}_{\gamma_2} = 0$. We will fit $\mathcal{F}_{\gamma_1}$ using the two-parameter model in Eq. (5) with the amplitude parameter replaced by $\mathcal{F}_c$ which is equivalent to $\Sigma_{crit}\kappa_c$ for a single lens–source pair.

3.3. Error estimation from SLICS

In order to estimate the error on the measured signal from observations, we use a large number of independent and representative lensing simulations from SLICS for each of the three

surveys. SLICS allows us to correctly account for the sampling variance, which was found to be the dominant source of noise in Kondo et al. (2019). The source sample of galaxies differs for each filament pair owing to our source selection that $z_B - z_f > 0.1$. For KV450 we can apply this source selection criteria accurately as the SLICS simulations include mock KV450 photometric redshifts that re-produce the scatter, bias and catastrophic outlier populations found in the KV450 data (Harnois-Déraps et al. 2018). For CFHTLenS and RCSLenS, this information is not encoded. We therefore create mocks from SLICS, modelling source samples for four different filament bins with $(z_{min}, z_{max}) = [0.1, 0.2]$, $[0.2, 0.3]$, $[0.3, 0.4]$, and $[0.4, 0.5]$, respectively. For each filament bin, we calculate the source galaxy redshift distribution $n(z)$, using Eq. (12) and the effective galaxy number density for sources with $z_B - z_{max} > 0.1$. We then populate 500 independent simulations using these distributions, and measure and combine the weighted shear and weight maps for each of the four filament bins. For KV450 we are able to verify that this binned approach is consistent to the unbinned methodology applied to the data using the KV450 SLICS simulations.

The covariance matrix of the signal is reweighted by the number of filament candidates for each survey, $n_{fil,survey}$, and estimated from the SLICS simulations as

$$\mathbf{Cov} = \frac{\bar{n}_{fil,sim}}{n_{fil,survey}} \frac{1}{N_{sim}-1} \sum_{k=1}^{N_{sim}} (\mathcal{F}_{\gamma_1}^k - \overline{\mathcal{F}_{\gamma_1}})(\mathcal{F}_{\gamma_1}^k - \overline{\mathcal{F}_{\gamma_1}})^T, \quad (19)$$

where $\overline{\mathcal{F}_{\gamma_1}}$ is the filament signal (Eq. (18)) averaged over all $N_{sim} = 500$ survey-specific SLICS simulations, and $\bar{n}_{fil,sim}$ is the average number of filament candidates in these simulations. The covariance is then used to calculate the χ^2 when estimating parameters in the filament model as

$$\chi_{model}^2 = (\mathcal{F}_{\gamma_1} - \mathcal{F}_{\gamma_1}^{fit})^T \mathbf{Cov}^{-1}(\mathcal{F}_{\gamma_1} - \mathcal{F}_{\gamma_1}^{fit}), \quad (20)$$

where $\mathcal{F}_{\gamma_1}^{fit} = \mathcal{F}_{\gamma_1}^{fit}(\mathcal{F}_c, r_c, r)$ is our filament model defined in Eq. (5), calculated on a fine grid of parameters $(\mathcal{F}_c, r_c)$. In analogy to Eq. (19), we also define a covariance for the $\mathcal{F}_{\gamma_2}$ component which serves as a systematic null-test for our analysis.

We found that a simple bootstrap error analysis of the data, where the set of maps are resampled with repetitions before stacking, underestimates the true measurement error. This approach misses the sampling variance term which, like Kondo et al. (2019), we find is a significant component to the error for small-area surveys such as KV450 and CFHTLenS.

3.4. Accounting for uncertainty in the redshift distributions

As discussed in Sect. 2.1, the probability distribution $\overline{p_s}(z_s, z_l)$ from Eq. (11) have not been calibrated for RCSLenS and CFHTLenS. A systematic uncertainty on the resulting $n(z_s)$ is thus expected. In order to take this into account, we use a nuisance parameter $\delta z_s = 0.1$ for RCSLenS and $\delta z_s = 0.04$ for CFHTLenS that captures the $p(z_s)$ uncertainty determined by Choi et al. (2016). For KV450 we use $\delta z_s = 0.025$ following Wright et al. (2019). We shift the $\overline{p_s}(z_s, z_l)$ by $\pm\delta z_s$ in Eq. (10) to yield two new functions $\overline{\Sigma_{crit}^{-1}}(z_l)^{\pm}$, and repeat the full measurement and error analysis using both the $\overline{\Sigma_{crit}^{-1}}(z_l)^+$ and $\overline{\Sigma_{crit}^{-1}}(z_l)^-$ calibration. We then estimate the likelihood of the data D given the model $(\mathcal{F}_c, r_c)$, assuming a prior on the uncertainty δz_s which
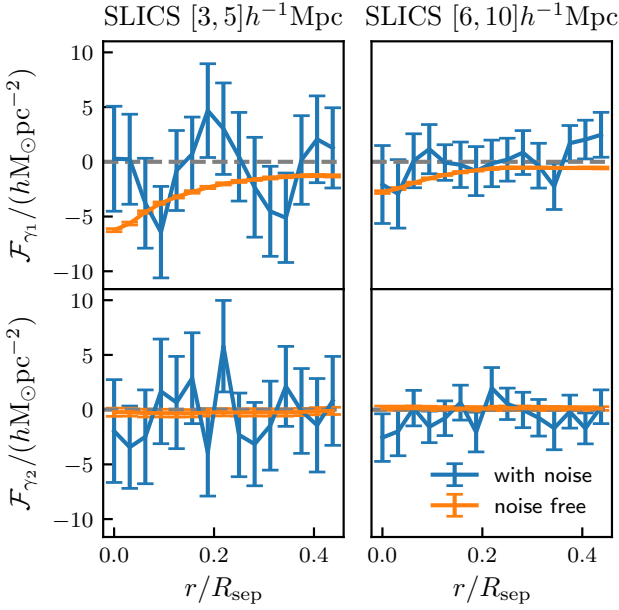
Fig. 2. Weighted shear measured between LRG pairs in the SLICS simulation of a random 400 deg^2 degree survey. *Left*: results from 3 to 5 h^{-1} Mpc filament candidates. *Upper panel*: average surface mass density $\mathcal{F}_{\gamma_1}$, and the *lower panel* shows the measured cross-shear component. On both panels, the blue data shows the result for a KiDS-like survey depth and shape noise, and the orange data points show the measurement for a noise-free simulation with the errorbar given by the error on the mean of all 158 realisations. *Right*: set of results from 6 to 10 h^{-1} Mpc filament candidates.

consists of 3 δ-functions and marginalised over as

$$\mathcal{L}(D|\mathcal{F}_\mathrm{c}, r_\mathrm{c}) = \mathcal{L}(D|\mathcal{F}_\mathrm{c}, r_\mathrm{c}, -\delta z_\mathrm{s}) + \mathcal{L}(D|\mathcal{F}_\mathrm{c}, r_\mathrm{c}, 0) + \mathcal{L}(D|\mathcal{F}_\mathrm{c}, r_\mathrm{c}, \delta z_\mathrm{s})$$

$$\propto \exp\left(-\frac{1}{2}\chi^2_{-\delta z_\mathrm{s}}\right) + \exp\left(-\frac{1}{2}\chi^2\right) + \exp\left(-\frac{1}{2}\chi^2_{\delta z_\mathrm{s}}\right). \quad (21)$$

A full marginalisation where many samples are taken at different redshift offsets, spanning the δz range, is unfortunately unfeasible given the complexity of the measurement pipeline.

4. Results

4.1. Filaments in SLICS

We validated our pipeline using the SLICS simulations of mock LOWZ lens galaxies and mock KiDS sources. We analysed both a noise-free catalogue and a catalogue with shape noise and mock photometric redshifts. The result is shown in Fig. 2 where the upper panels show measurements of $\mathcal{F}_{\gamma_1}$, and the lower panels show measurements of $\mathcal{F}_{\gamma_2}$. The left and right columns correspond to results from the 3–5 h^{-1} Mpc and 6–10 h^{-1} Mpc filament candidates, respectively.

For the noise-free simulations, we find that $\mathcal{F}_{\gamma_2}$ is consistent with zero for both the 3–5 h^{-1} Mpc and 6–10 h^{-1} Mpc length filaments. This demonstrates that our nulling procedure correctly removes the contribution from the LRG haloes in the analysis. However, for the simulations with shape noise, both the $\mathcal{F}_{\gamma_1}$ and $\mathcal{F}_{\gamma_2}$ measurements are consistent with zero, which suggests that even though KV450 is deeper than the KiDS-450 data simulated in SLICS, we should not expect a significant detection from KiDS alone. As the variance in the noise-free simulation reflects the level of sample variance, we also report that, by measuring

the noise level from these two sets of simulations, the sample variance is comparable with the shape noise.

Constraining the parameters of Mead et al. (2010) model with the noise-free SLICS results we find $\mathcal{F}_\mathrm{c}^{3-5} = 5.61 \pm 0.55\,h\,M_\odot\,\mathrm{pc}^{-2}$, $r_\mathrm{c}^{3-5} = 0.40 \pm 0.04\,h^{-1}\,\mathrm{Mpc}$, $\mathcal{F}_\mathrm{c}^{6-10} = 2.25 \pm 0.14\,h\,M_\odot\,\mathrm{pc}^{-2}$, and $r_\mathrm{c}^{6-10} = 1.12 \pm 0.08\,h^{-1}\,\mathrm{Mpc}$. The $\chi^2_{3-5} = 16.33$ and $\chi^2_{6-10} = 15.42$ demonstrate that the model is a good fit to the data ($\nu = 13$ degrees of freedom). We find that the surface mass density of the filament is a factor of 2.5 smaller for the 6–10 h^{-1} Mpc filament and will therefore be more challenging to detect using gravitational lensing.

With the noise-free simulations we are able to analyse whether our signal depends on the redshift of the filament. We constrain the amplitude $\mathcal{F}_\mathrm{c}$ and the scale r_c parameters of the filament model for 4 redshift quantiles of the SLICS LOWZ filament samples using the same background sources, with the result shown in Fig. 3. The choice of parameterisation on the axes is motivated by the filament model equation as well as for visual simplicity. Here we see significant differences between the samples which could be caused by an evolution in the bias of the LOWZ-like galaxy samples in the SLICS mocks, or the evolution of the filament density field. Given the different source redshift distributions of the three lensing surveys (see Fig. 1) which makes the effective redshift of the average lens differ, this result suggests that we should not necessarily expect the results of these surveys to agree perfectly.

### 4.2. The detection of filaments with KV450, RCSLenS and CFHTLenS

Figure 4 presents our filament shear measurements and constraints on the two parameters of the filament model (Eq. (5)) for physical pairs, our filament candidates (upper panels), and non-physical pairs, our control sample (lower panels). The left panel shows the nulled $\mathcal{F}(r)$ shear signal as a function of the distance from the centre of the filament measured in units of $h\,M_\odot\,\mathrm{pc}^{-2}$. The result is presented for each lensing survey. We also show the measurements from the three-surveys combined using inverse variance weighting. The blue data points are a measurement of $\mathcal{F}_{\gamma_1}$, whereas the orange data points show the null-test $\mathcal{F}_{\gamma_2}$. The shaded region corresponds to the statistical noise from our fiducial measurements, and the capped errorbars correspond to the systematic uncertainty captured by the photometric redshift bias nuisance parameter δz (see Sect. 3.4). The right panel shows the 68% and 95% confidence region of parameters $\mathcal{F}_\mathrm{c}$ and r_c in Mead et al. (2010) filament model. These estimated parameters can be compared to the best-fit parameter from the noise-free SLICS analysis in Sect. 4.1 which is also represented by the cross in the right panel. We note that the noise-free SLICS best-fit is consistent with all three surveys. We also present joint constraints from the combined signal using a block covariance

$$\mathrm{Cov}_{\mathrm{all}} = \begin{pmatrix} \mathrm{Cov}_{\mathrm{CF}} & 0 & 0 \\ 0 & \mathrm{Cov}_{\mathrm{RC}} & 0 \\ 0 & 0 & \mathrm{Cov}_{\mathrm{KV}} \end{pmatrix} \quad (22)$$

and extended data vector $\mathcal{F}_{\mathrm{ext}} = (\mathcal{F}_{\mathrm{CF}}, \mathcal{F}_{\mathrm{RC}}, \mathcal{F}_{\mathrm{KV}})^\mathrm{T}$, providing an estimate of the average filament profile from all the filament candidates across the three surveys. Equation (22) assumes that the surveys are uncorrelated, which is a good approximation to make given the lack of overlap between the different surveys.

To quantify the significance of our measurements, we use the likelihood ratio test between the null hypothesis H_0 and the
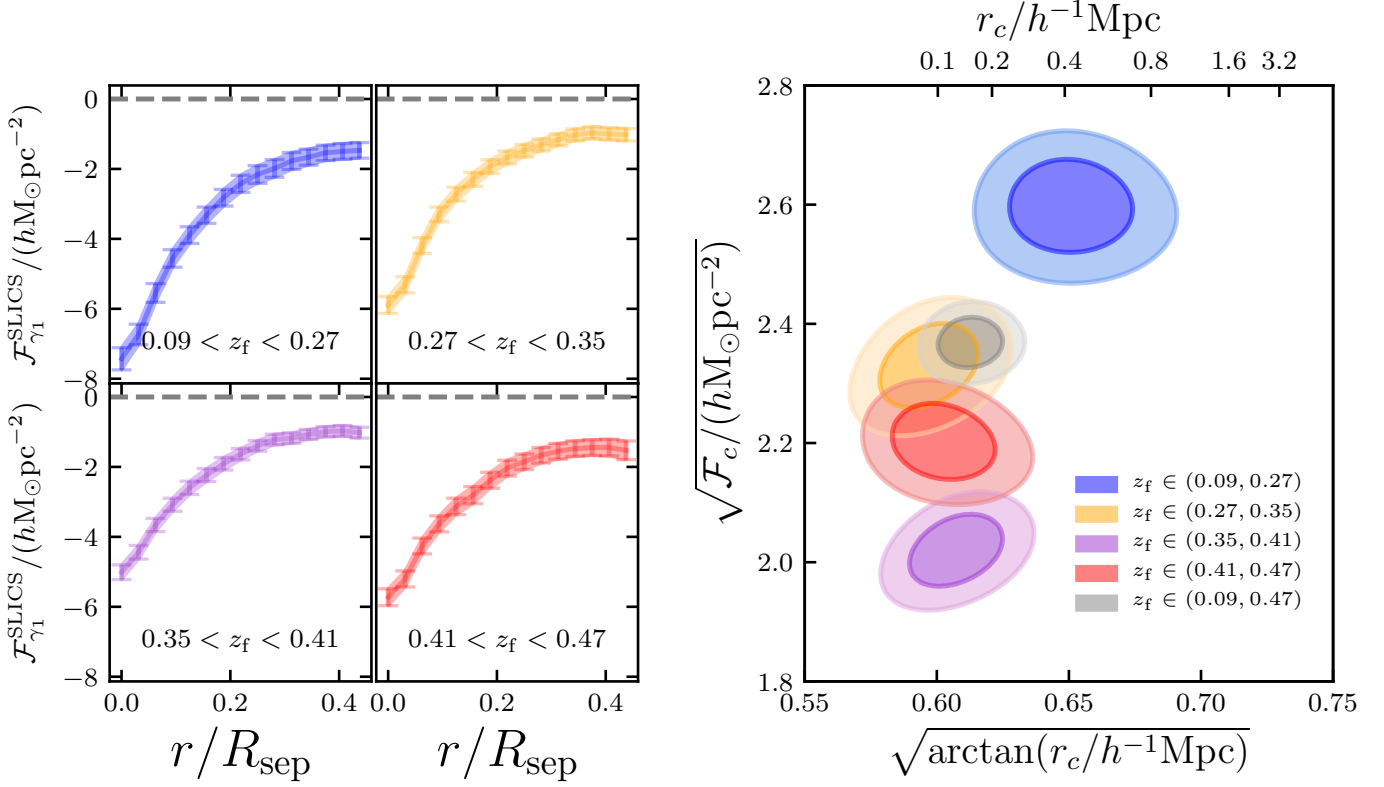
Fig. 3. Redshift evolution of the filament signal in the noise-free SLICS simulation. *Left panel*: $\mathcal{F}_{\gamma_1}$ signal measured from filament candidates in SLICS for four redshift quantiles. *Right panel*: 68% and 95% confidence region of the model parameters $(\mathcal{F}_c, r_c)$ from the corresponding signal in the *left panel*, with the result from all samples combined shown in grey.

filament model H_1, where the likelihood ratio LR is

$$\text{LR}(\mathcal{F}(r)) = \frac{\sup\limits_{\theta \in B_1} \mathcal{L}(\theta | \mathcal{F}(r))}{\sup\limits_{\theta \in B_0} \mathcal{L}(\theta | \mathcal{F}(r))}, \quad (23)$$

where B_0 and B_1 are the parameter space in each hypothesis, i.e., B_0 has no free parameters and $B_1 = \{\mathcal{F}_c, r_c\}$. By Wilks' theorem (Wilks 1938; Williams 2001), the deviance defined as Dev $= 2 \ln \text{LR}$ has an asymptotic chi-squared distribution with $\dim(B_1) - \dim(B_0) = 2$ degrees of freedom when H_0 is true. Estimating the maximum likelihoods from χ^2_{null} and $\chi^2_{\text{model,min}}$ using Eq. (21) and computing the deviance, we report the significance level for each individual survey as well as the combined analysis in Table 3. The reported $\chi^2_{\text{min,model}}$ suggests our model is a reasonable fit to the data in all cases even for KV450, where $p(\chi^2 < 7.40 | \nu = 13) = 0.12$. We find the best-fit model parameters for $\mathcal{F}_{\gamma_1}$ from all three surveys combined as $\mathcal{F}_c = 10.5 \pm 2.9 \, h \, M_\odot \, \text{pc}^{-2}$ and $r_c = 0.4^{+0.2}_{-0.1} \, h^{-1} \, \text{Mpc}$. We note that, the majority of the detection derives from CFHTLenS alone with a 3.1σ detection. Combining all three surveys we measure a 3.4σ detection of the filament weak lensing signal. CFHTLenS is the most constraining survey as it combines both survey depth with significant SDSS overlap. KV450, with roughly half the source density of CFHTLenS, and RCSLenS, with roughly 20% of the source density, will only start to add significant constraining power with the inclusion of additional overlapping SDSS area.

Our control sample of "non-physical pairs" (NP) were selected to be pairs of lens galaxies with projected separations $3-5 \, h^{-1} \, \text{Mpc}$, but distant in redshift space $(0.033 < \Delta z < 0.04)$.

These non-physical pairs would not be connected by a filament, hence providing an important validation of our nulling approach to isolate the filament signal. We find that the measured signal for $\mathcal{F}_{\gamma_{1,2}}$ is consistent with zero for all surveys and the combined survey as shown in Table 3 and the lower panel of Fig. 4.

For consistency with other analyses in the literature we also analysed 27 880 filament pairs in LOWZ that have a physical separation of $6-10 \, h^{-1} \, \text{Mpc}$. In contrast to other studies, we do not detect a significant signal for these larger-separation filaments in any of the surveys individually. In combination we find a weak signal at 1.6σ significance, with $\mathcal{F}_c = 1.3 \pm 0.6$. The half-maximum radius of the density profile, r_c, is, however, unconstrained.

5. Conclusions and discussion

In this paper, we present a 3.4σ detection of filamentary structure connecting luminous red galaxies separated by $3-5 \, h^{-1} \, \text{Mpc}$. Through a series of null tests we have verified the robustness of this result. Our work extends the analysis presented in C16 by improving the methodology to null the weak lensing signal from the LRGs in order to isolate the weak lensing distortions induced by the filamentary structure alone. We note that this nulling method cannot distinguish between a pair of spherical haloes joined by a cylinder of matter, or two elliptical haloes which extend towards each other. Higuchi et al. (2014) shows that there is no hard line between a filament and its corresponding halo, with haloes typically extending along the filament. As we find a strong nulled signal on scales much larger than the typical $(\sim 1 \, h^{-1} \, \text{Mpc})$ virial radius of the LRGs (Parejko et al. 2013), we would argue that it is unlikely to originate from two perfectly
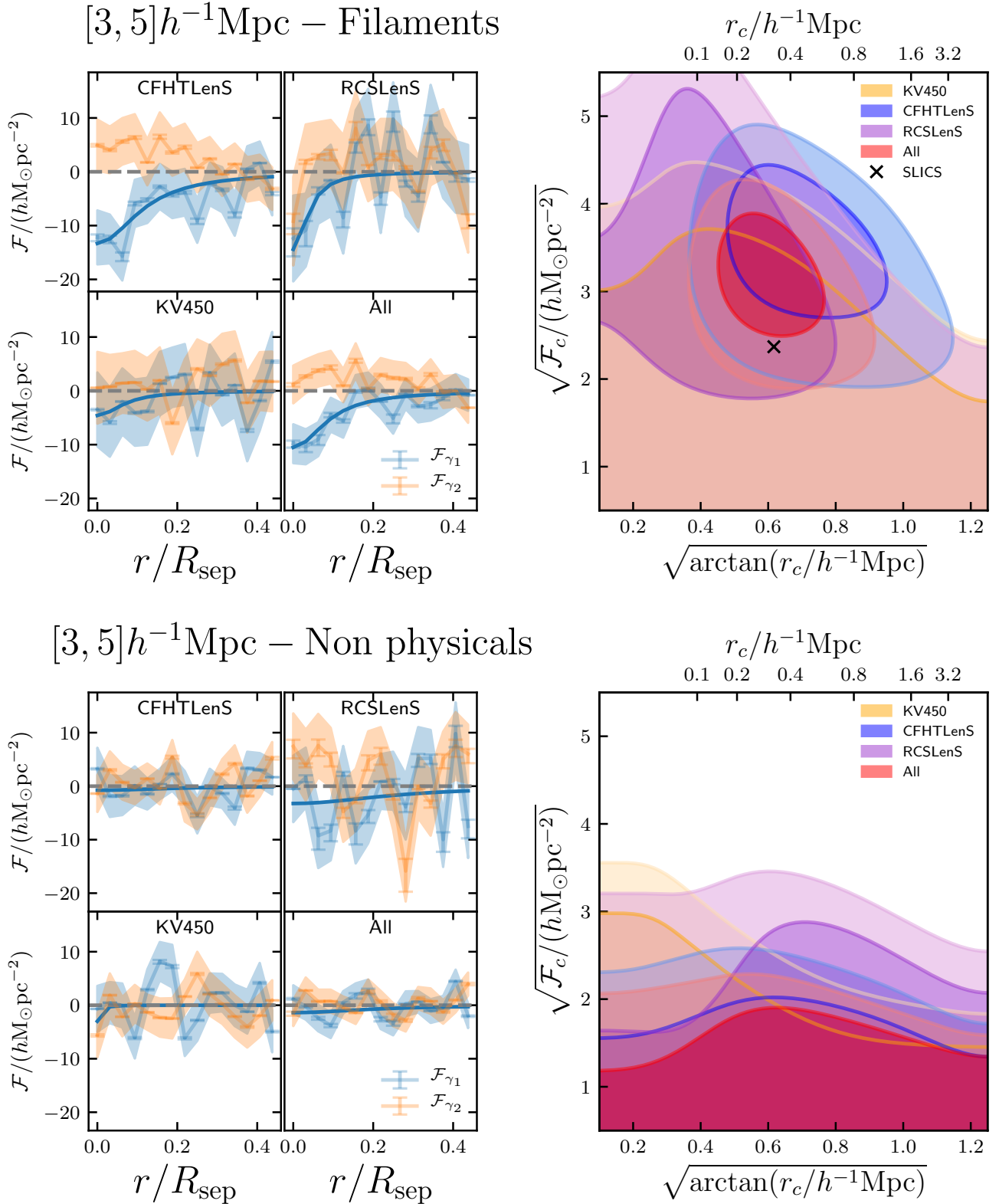
Fig. 4. The detection of the cosmic web between neighbouring luminous red galaxies as detected through the weak lensing of background galaxies from different lensing surveys. *Left*: x-axis is the distance measured perpendicular to the filament axis scaled such that 1 is equivalent to the projected separation between the pair of LRGs. The y-axis is the nulled shear signal where $\mathcal{F}_{\gamma_1}$ (blue data points) measures the average surface mass density of the filament, and $\mathcal{F}_{\gamma_2}$ is expected to be consistent with zero and hence serves as a null test. *Lower right small panel*: measurements from the three-surveys combined using inverse variance weighting. We note that this additional panel is purely for illustration, however, as our joint survey-constraints on the filament model are derived from a combination of the surveys on the likelihood-level. *Right*: estimated parameters in the filament density model Eq. (5) from the stacked signal for all surveys individually and their combination. *Upper*: results from 3~5 h^{-1} Mpc Physical Pairs, our filament candidates; *Lower*: results from 3~5 h^{-1} Mpc non-physical Pairs, our control sample.

Table 3. χ^2 value and p-value for all computed signals from each individual survey and their combination.

		CFHTLenS	RCSLenS	KV450	All
	$\mathcal{F}_c/(h\,M_\odot\,\mathrm{pc}^{-2})$	$13.3^{+4.1}_{-4.0}$	$14.4^{+8.5}_{-7.6}$	$4.6^{+5.9}_{-4.5}$	$10.5^{+2.9}_{-2.8}$
	$r_c/(h^{-1}\,\mathrm{Mpc})$	$0.5^{+0.4}_{-0.2}$	$0.2^{+0.3}_{-0.1}$	$-$	$0.4^{+0.2}_{-0.1}$
	$\chi^2_{\mathrm{min,model}}$	12.2	11.6	7.5	40.4
PP	$\chi^2_{\mathrm{min,null},\mathcal{F}_{\gamma_1}}$	24.6	15.6	8.1	55.0
	$\sigma_{\mathcal{F}_{\gamma_1}}$	3.08	1.49	0.35	3.40
	$\chi^2_{\mathrm{min,null},\mathcal{F}_{\gamma_2}}$	6.8	6.78	2.61	22.06
	$\sigma_{\mathcal{F}_{\gamma_2}}$	0.05	0.05	2e-4	2e-3
	$\chi^2_{\mathrm{min,null},\mathcal{F}_{\gamma_1}}$	9.2	20.0	19.3	53.8
	$\sigma_{\mathcal{F}_{\gamma_1}}$	0.17	1.38	1.28	1.36
NP	$\chi^2_{\mathrm{min,null},\mathcal{F}_{\gamma_2}}$	12.3	20.7	5.8	43.0
	$\sigma_{\mathcal{F}_{\gamma_2}}$	0.44	1.45	0.02	0.59

Notes. For each survey, PP means physical pair and NP stands for non-physical pair. Both NP and $\mathcal{F}_{\gamma_2}$ serve as null tests for our analysis. For the combined signals, the degree of freedom is $\nu = 45 - 2$. We also note that r_c is unconstrained by KV450.

aligned haloes (see Xia et al. 2017). But nevertheless we prefer to refer to our detection as that of filamentary structure, rather than that of a filament per se.

Previous studies have focused on LRGs separated by $6-10\,h^{-1}$ Mpc. Using all three lensing surveys (KV450, CFHTLenS and RCSLenS), we do not detect a significant signal for these larger-separation filaments in either the surveys individually, or in combination. This is in contrast to the significant 5σ weak lensing detection of $6-10\,h^{-1}$ Mpc separation filaments reported by Epps & Hudson (2017) using the same CFHTLenS dataset that has been analysed in this study. We report that we are unable to reproduce their result, even when adopting the same methodology. In comparison to C16, we find no comparable detection to their reported $\sim4\sigma$ detection. As we have shown that sampling variance makes a significant contribution to the overall error budget, the increase by a factor of 5 in the number of filaments studied by C16, in contrast to this analysis, is key to their detection, even though the C16 lensing source galaxy density is significantly shallower than the source densities of KV450, CFHTLenS and RCSLenS. Neither Epps & Hudson (2017) nor C16 constrain the parameters of the Mead et al. (2010) filament model, but in the case of C16 we can compare the amplitudes of the measured signals. When adopting the C16 nulling approach, we find the two shear measurements to be fully consistent. The mean amplitude of our measurement is about four times larger than the amplitude reported in Kondo et al. (2019) (see discussion in Appendix A). Given our error budget, however, the results are consistent.

Authors de Graaff et al. (2019) calculate the average density $\bar{\kappa}$ between galaxy pairs separated by $6-14\,h^{-1}$ Mpc using a CMB lensing convergence map, finding $\rho_0 \approx 5.5 \pm 2.9\,\bar{\rho}(z)$. This estimate assumes that the matter density follows a cylindrical filament model, with density

$$\rho(\ell, r_\perp) = \rho_0 \exp\left(-\frac{r_\perp^2}{2\sigma^2}\right)\exp\left(-\frac{\ell^2}{2\sigma^2}\right), \quad (24)$$

where ℓ defines the size of the filament in the line-of-sight direction, $r_\perp$ defines the distance perpendicular to the filament axis on the projected sky and σ is the intrinsic width. Integrating this density model over the line-of-sight, we can relate this to the

surface mass density at the centre of the filament $\mathcal{F}_c$ as

$$\mathcal{F}_c = \int \rho(\ell, 0)\,\mathrm{d}\ell = \sqrt{2\pi}\sigma\rho_0. \quad (25)$$

For the value $\sigma = 1.5\,h^{-1}$ Mpc adopted by de Graaff et al. (2019), and which is our best-fit amplitude parameter $\mathcal{F}_c$, we find $\rho_0^{3-5} = (15.1 \pm 4.1)\,\bar{\rho}(z)$ for the $3-5\,h^{-1}$ Mpc filament sample at the average filament redshift $z = 0.299$. For the $6-10\,h^{-1}$ Mpc filament sample we find $\rho_0^{6-10} = (1.9 \pm 0.9)\,\bar{\rho}(z)$, which is consistent with the de Graaff et al. (2019) result. Adapting the Mead et al. (2010) filament model, we can also integrate the model over the perpendicular distance and calculate the total mass enclosed between the two LRGs as

$$M_{\mathrm{fil}}(r_c, \mathcal{F}_c, R_{\mathrm{sep}}) = R_{\mathrm{sep}} \times 2\int_0^\infty \mathcal{F}(r)\,\mathrm{d}r = \pi\,r_c\,R_{\mathrm{sep}}\,\mathcal{F}_c. \quad (26)$$

Taking the best-fit parameters $\mathcal{F}_c$ and r_c for $3-5\,h^{-1}$ Mpc measurement, we find $M_{\mathrm{fil}} = 4.9 \pm 2.0 \times 10^{13}\,h^{-1}\,M_\odot$. It is worth noting that this estimate is based on the approximation that the deflection potential vanishes along the filament major axis. A more detailed analysis would attempt to obtain the excess mass map under the framework of galaxy-galaxy-galaxy lensing (Simon et al. 2008, 2019) but with a much larger separation of galaxy pairs.

Looking forward to upcoming deep weak lensing surveys, such as the European Space Agency's *Euclid* mission[5] and the Large Synoptic Survey Telescope (LSST[6]), and deep spectroscopic surveys such as the Dark Energy Spectroscopic Instrument (DESI[7]), the methodology that we present in this paper could be used to probe filamentary structure as a function of LRG mass and redshift. The combination of overlapping weak lensing surveys and spectroscopic surveys will provide the optimal datasets with which to fully explore the cosmic web.

References

Alam, S., Albareti, F. D., Allende Prieto, C., et al. 2015, ApJS, 219, 12
Amon, A., Heymans, C., Klaes, D., et al. 2018, MNRAS, 477, 4285
Aragón-Calvo, M. A., van de Weygaert, R., & Jones, B. J. T. 2010, MNRAS, 408, 2163
Bartelmann, M., & Schneider, P. 2001, Phys. Rep., 340, 291
Benítez, N. 2000, ApJ, 536, 571
Bond, J. R., Kofman, L., & Pogosyan, D. 1996, Nature, 380, 603
Bregman, J. N. 2007, ARA&A, 45, 221
Briel, U. G., & Henry, J. P. 1995, A&A, 302, L9
Cheng, H., & Gupta, K. C. 1989, ASME Trans. Ser. E: J. Appl. Mech., 56, 139
Choi, A., Heymans, C., Blake, C., et al. 2016, MNRAS, 463, 3737
Clampitt, J., Miyatake, H., Jain, B., & Takada, M. 2016, MNRAS, 457, 2391
Colberg, J. M., Krughoff, K. S., & Connolly, A. J. 2005, MNRAS, 359, 272
Colless, M., Dalton, G., Maddox, S., et al. 2001, MNRAS, 328, 1039
de Graaff, A., Cai, Y.-C., Heymans, C., & Peacock, J. A. 2019, A&A, 624, A48
Dietrich, J. P., Werner, N., Clowe, D., et al. 2012, Nature, 487, 202
Dolag, K., Meneghetti, M., Moscardini, L., Rasia, E., & Bonaldi, A. 2006, MNRAS, 370, 656
Dvornik, A., Hoekstra, H., Kuijken, K., et al. 2018, MNRAS, 479, 1240
Eardley, E., Peacock, J. A., McNaught-Roberts, T., et al. 2015, MNRAS, 448, 3665
Ebeling, H., Barrett, E., & Donovan, D. 2004, ApJ, 609, L49
Epps, S. D., & Hudson, M. J. 2017, MNRAS, 468, 2605
Harnois-Déraps, J., & van Waerbeke, L. 2015, MNRAS, 450, 2857
Harnois-Déraps, J., Amon, A., Choi, A., et al. 2018, MNRAS, 481, 1337
Heymans, C., Van Waerbeke, L., Bacon, D., et al. 2006, MNRAS, 368, 1323
Heymans, C., Van Waerbeke, L., Miller, L., et al. 2012, MNRAS, 427, 146
Higuchi, Y., Oguri, M., & Shirasaki, M. 2014, MNRAS, 441, 745
Hildebrandt, H., Erben, T., Kuijken, K., et al. 2012, MNRAS, 421, 2355
Hildebrandt, H., Choi, A., Heymans, C., et al. 2016, MNRAS, 463, 635
Hildebrandt, H., Viola, M., Heymans, C., et al. 2017, MNRAS, 465, 1454
Hildebrandt, H., Köhlinger, F., van den Busch, J. L., et al. 2018, A&A, accepted, https://doi.org/10.1051/0004-6361/201834878
Kondo, H., Miyatake, H., Shirasaki, M., Sugiyama, N., & Nishizawa, A. J. 2019, ArXiv e-prints [arXiv:1905.08991]
Kull, A., & Böhringer, H. 1999, A&A, 341, 23
Macciò, A. V., Dutton, A. A., van den Bosch, F. C., et al. 2007, MNRAS, 378, 55
Mandelbaum, R., Hirata, C. M., Seljak, U., et al. 2005, MNRAS, 361, 1287
Mead, J. M. G., King, L. J., & McCarthy, I. G. 2010, MNRAS, 401, 2257
Miller, L., Heymans, C., Kitching, T. D., et al. 2013, MNRAS, 429, 2858
Parejko, J. K., Sunayama, T., Padmanabhan, N., et al. 2013, MNRAS, 429, 98
Pimbblet, K. A., & Drinkwater, M. J. 2004, MNRAS, 347, 137
Ross, A. J., Percival, W. J., Sánchez, A. G., et al. 2012, MNRAS, 424, 564
Schneider, P., & Watts, P. 2005, A&A, 432, 783
Simon, P., Watts, P., Schneider, P., et al. 2008, A&A, 479, 655
Simon, P., Saghiha, H., Hilbert, S., et al. 2019, A&A, 622, A104
Springel, V., White, S. D. M., Jenkins, A., et al. 2005, Nature, 435, 629
Tanimura, H., Hinshaw, G., McCarthy, I. G., et al. 2019, MNRAS, 483, 223
Velander, M., Kuijken, K., & Schrabback, T. 2011, MNRAS, 412, 2665
Velander, M., van Uitert, E., Hoekstra, H., et al. 2014, MNRAS, 437, 2111
Werner, N., Finoguenov, A., Kaastra, J. S., et al. 2008, A&A, 482, L29
Wilks, S. S. 1938, Ann. Math. Stat., 9, 60
Williams, D. 2001, Weighing the Odds: A Course in Probability and Statistics (Cambridge: Cambridge University Press)
Wright, A. H., Hildebrandt, H., Kuijken, K., et al. 2019, A&A, 632, A34
Wright, C. O., & Brainerd, T. G. 2000, ApJ, 534, 34
Xia, Q., Kang, X., Wang, P., et al. 2017, ApJ, 848, 22
Zehavi, I., Zheng, Z., Weinberg, D. H., et al. 2011, ApJ, 736, 59
Zel'dovich, Y. B. 1970, A&A, 5, 84

Appendix A: Remarks on the nulling technique

In this appendix, we review the C16 nulling technique and develop an improved methodology to isolate the weak lensing signal from filaments. To explain the motivation behind nulling, we start with a single circularly symmetric halo positioned at the origin $(0,0)$, for which the complex shear is given by

$$\gamma(\boldsymbol{r}) = \gamma(r, \theta) = \gamma_1 + \mathrm{i}\gamma_2 = -(\bar{\kappa} - \kappa)\mathrm{e}^{2\mathrm{i}\theta}, \tag{A.1}$$

where $\bar{\kappa}$ is the mean convergence inside r. We define its counterpart γ^{c} as the complex shear at the same radial position, with a clockwise rotation of $90°$, such that

$$\gamma^{\mathrm{c}}(\boldsymbol{r}) \equiv \gamma\left(r, \theta + \frac{\pi}{2}\right) = -\gamma(r, \theta). \tag{A.2}$$

The counterpart is therefore able to "null" the shear, as $\gamma^{\mathrm{c}}(\boldsymbol{r}) + \gamma(\boldsymbol{r}) = 0$.

For a two-halo system as shown in Fig. A.1, the shear at each position (r, θ) is composed with the shear from halo h_1 and the shear from halo h_2. We can write this as

$$\gamma(r, \theta) = \gamma_{\mathrm{h}_1}(t, \varphi) + \gamma_{\mathrm{h}_2}(s, \phi), \tag{A.3}$$

where the co-ordinates (t, φ) are defined with halo h_1 at the origin, and the co-ordinates (s, ϕ) are defined with halo h_2 at the origin. Starting from position $P_0 = (r_0, \theta_0)$, shear is given by

$$P_0 : \gamma(r_0, \theta_0) = \gamma_{\mathrm{h}_1}(t_0, \varphi_0) + \gamma_{\mathrm{h}_2}(s_0, \phi_0). \tag{A.4}$$

A clockwise rotation around halo h_1 by $90°$ takes us to position P_1 at (r_1, θ_1). The shear here is given by

$$P_1 : \gamma(r_1, \theta_1) = \gamma_{\mathrm{h}_1}\left(t_0, \varphi_0 + \frac{\pi}{2}\right) + \gamma_{\mathrm{h}_2}(s_1, \phi_1). \tag{A.5}$$

At position P_1, we see the shear contribution from halo h_1 is the counterpart to the shear contribution from halo h_1 at position P_0. We next rotate around halo h_2 by $90°$ to position $P_2 = (r_2, \theta_2)$, where the shear is given by

$$P_2 : \gamma(r_2, \theta_2) = \gamma_{\mathrm{h}_1}(t_2, \varphi_2) + \gamma_{\mathrm{h}_2}\left(s_1, \phi_1 + \frac{\pi}{2}\right). \tag{A.6}$$

Similarly another $90°$ rotation about halo h_1 (see Fig. A.2) to position P_3 gives

$$P_3 : \gamma(r_3, \theta_3) = \gamma_{\mathrm{h}_1}\left(t_2, \varphi_2 + \frac{\pi}{2}\right) + \gamma_{\mathrm{h}_2}(s_3, \phi_3). \tag{A.7}$$

We note that, after another $90°$ rotation about halo h_2, we come to position P_4 which is our starting point P_0. The sum of the shear from position P_0, P_1, P_2 and P_3 is given by
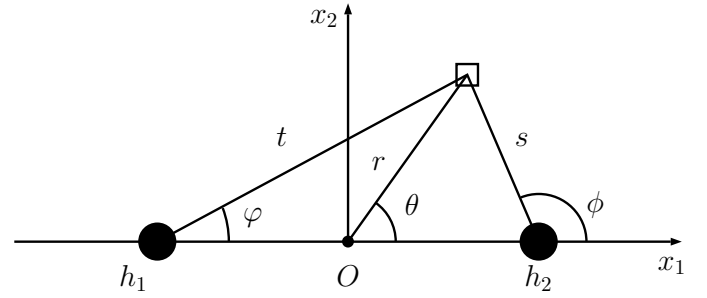
$$\sum_{i=0}^{3} \gamma(r_i, \theta_i) = \gamma_{\mathrm{h}_2}(s_0, \phi_0) + \gamma_{\mathrm{h}_2}(s_3, \phi_3) \tag{A.8}$$

$$= \gamma_{\mathrm{h}_2}\left(s_3, \phi_3 + \frac{\pi}{2}\right) + \gamma_{\mathrm{h}_2}(s_3, \phi_3) = 0. \tag{A.9}$$
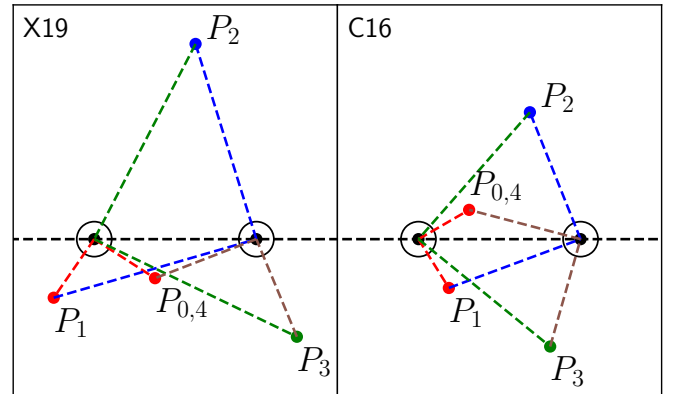
If we now add in a filament shear γ_{f} such that at each position $\gamma = \gamma_{\mathrm{f}} + \gamma_{h_1} + \gamma_{h_2}$, then

$$\sum_{i=0}^{3} \gamma(r_i, \theta_i) = \gamma_{\mathrm{f}}(r_0, \theta_0) + \gamma_{\mathrm{f}}(r_1, \theta_1) + \gamma_{\mathrm{f}}(r_2, \theta_2) + \gamma_{\mathrm{f}}(r_3, \theta_3). \tag{A.10}$$

As we expect the filament shear profile to be symmetric about the horizontal axis, we also sum over the shear from positions

Fig. A.1. The bipolar configuration for two haloes centred symmetrically about origin O at h_1 and h_2.

Fig. A.2. Illustration of the nulling technique. Every two line segments with the same colour represents an anti-clockwise rotation with respect to one halo. *Right*: configuration described in C16. *Left*: our adopted "X19" configuration which starts below the horizontal axis.

P_0', P_1', P_2' and P_3' that are reflections of P_0, P_1, P_2 and P_3 about the horizontal axis respectively, in order to get the average shear value at any distance away from filament axis. We therefore define the nulling operator $\mathcal{N}$ as

$$\mathcal{N}[\gamma(r_0, \theta_0)] = \frac{1}{2}\left(\sum_{i=0}^{3} \gamma(r_i, \theta_i) + \sum_{i=0}^{3} \gamma(r_i', \theta_i')\right). \tag{A.11}$$

It is interesting to note that the above equations also apply when two halos are of different masses given their circular symmetry.

In Fig. A.2 we show two configurations for nulling. C16 chose to start P_0 above the horizontal axis and our work starts P_0 below the horizontal axis. We investigate the difference between these two approaches by first constructing a noise-less shear map from two NFW halo profiles using Eq. (14) in Wright & Brainerd (2000) with $M_{\mathrm{vir}} = 10^{13} \, h^{-1} \, M_{\odot}$ and assuming a mass–concentration relation from Macciò et al. (2007). We assume both haloes are located at $z = 0.3$ with background sources at redshift 0.7, close to the mean value of KiDS. The resultant γ_1 map is shown in the top-left panel of Fig. A.3.

For each pixel (x_1, x_2) on the map, we calculate $\mathcal{N}[\gamma_i(x_1, x_2)]$, and show in the top-right panel in Fig. A.3, the average of the sum along the horizontal axis, i.e., $\gamma_1^{\mathrm{null}}(r) = \sum_{x=x_{\mathrm{min}}}^{x_{\mathrm{max}}} \mathcal{N}[\gamma_1(x_1, x_2)]/(x_{\mathrm{max}} - x_{\mathrm{min}} + 1)$. In the lower-right panel in Fig. A.3, we show the resulting $\mathcal{N}[\gamma_2(x_1, x_2)]$. As expected, the sum of nulling pixels are zeros (note the $10^{-16}/10^{-18}$ on the y-axis). In the middle panel we repeat the analysis with the inclusion of a fiducial filament modelled using the power-law profile model in Eq. (5). The filament contribution to the shear $\gamma_1^{\mathrm{fil}}(r)$ is
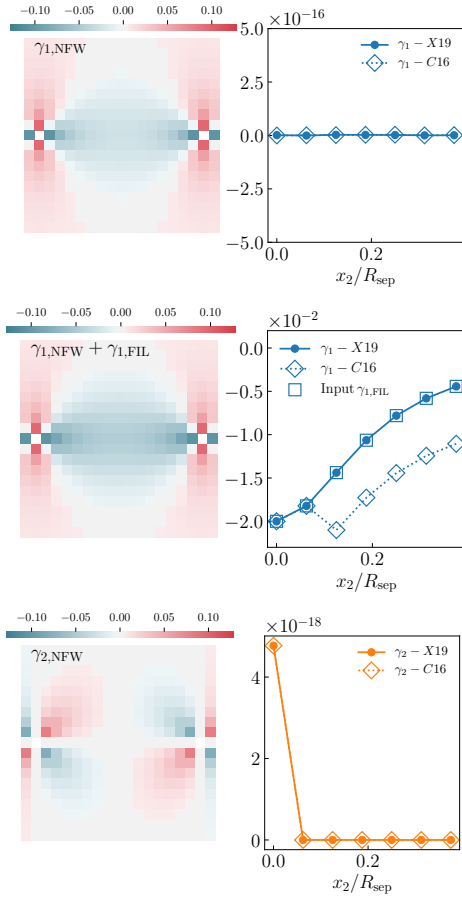
Fig. A.3. *Left panel*: shear maps from two NFW halos with or without fiducial filaments. *Top row*: γ_1 map generated by two NFW haloes only, while the *middle row* shows the γ_1 map with the addition of a fiducial filament profile. *Lowest row*: γ_2 map generated by two NFW haloes. it Right panel: results of the nulling procedure corresponding to the shear map on the left. In the *top row*, we see under both the X19 configuration (solid line) and C16's (dashed line), the resulting signal is consistent with zero. When adding a fiducial filament profile, in the *middle row*, we see our X19 configuration correctly recovers the input value whereas the C16 configuration is biased on large scales. In the *lower row*, we verify that both configurations null the γ_2 signal from two NFW haloes.

included in the 2D shear map as a power-law, symmetric about the x_1-axis (at $x_2 = 0$) with $k_c = 0.02$ and $r_c = 0.4\,h^{-1}$ Mpc. These parameters were chosen to roughly replicate previous studies (Dolag et al. 2006), in order to model the true signal contrast in observations. If the nulling method is precise, we would expect the nulled filament signal measured from the map, $\gamma_1^{\mathrm{null}}(r)$ to recover the input shear from the filament, $\gamma_1^{\mathrm{fil}}(r)$, irrespective of the nulling method used. The middle-right panel shows that this is indeed the case, with our nulling method. The nulling method in C16, however, recovers a lower expectation value for the shear induced by the filament. This difference results from the C16 configuration. As shown in Eq. (A.10), for the C16 configuration, since P_0 and P_1 are both in the filament region, the nulling operator effectively mixes scales. This has an effect in producing a significant signal on large scales which does not reflect the underlying filament density profile. As P_1, P_2 and P_3 in our adopted configuration lies outside the bridge between two haloes, $\gamma_f(r_1, \theta_1) + \gamma_f(r_2, \theta_2) + \gamma_f(r_3, \theta_3)$ is negligible. This

enables us to recover the density profile accurately. We note that Kondo et al. (2019) adopted the C16 estimator but in their Eq. (9) (the equivalent of our Eq. (A.11)), they included an additional factor of 4 in the denominator, which, in our test-case in Fig. A.3 would result in the underestimation of the filament signal by a factor of 4.

Appendix B: Remarks on the spherical rotation
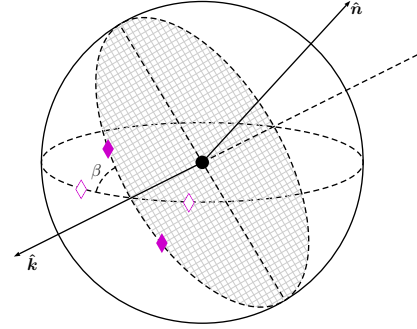
Fig. B.1. Illustration of the spherical rotation for filament pairs (solid pink diamonds). Open symbols are the rotated positions.

Here we detail the spherical rotation used in Sect. 3.2 to project all filaments onto the same reference frame. As illustrated in Fig. B.1, we rotate all galaxies about a given axis so that the filament (the shorter arc connected by solid pink diamonds) is transformed to lie horizontally on the equator (hollow pink diamonds). To do this, we first transfer the right ascension and declination onto a 3D vector on a unit sphere, such that their positions are $\boldsymbol{g}_1$ and $\boldsymbol{g}_2$. The normal vector is defined as $\hat{\boldsymbol{n}} = \boldsymbol{g}_1 \times \boldsymbol{g}_2$. Noting the rotation axis lies on the equator and is perpendicular to the normal vector, we can write down the rotation axis $\hat{\boldsymbol{k}}$ and angle β using components of $\hat{\boldsymbol{n}}$, so that

$$\hat{\boldsymbol{k}} = \frac{(n_2, -n_1, 0)^{\mathrm{T}}}{\sqrt{n_1^2 + n_2^2}}, \tag{B.1}$$

$$\beta = \arccos(n_3). \tag{B.2}$$

We note that by defining $\boldsymbol{g}_1$ to be always on the left of $\boldsymbol{g}_2$, there is no ambiguity in the definition of the rotation axis, and the rotation angle will always lie between $\left[0, \frac{\pi}{2}\right]$. Rodrigues' rotation formula (Cheng & Gupta 1989) then allows us to rotate every point on the sky to the desired frame where the filament pair now lies on the equator, such that for each source galaxy at position $\boldsymbol{g}_s$, the new position is at:

$$\boldsymbol{g}_{\mathrm{new}} = \boldsymbol{g}_s \cos\beta + \sin\beta(\hat{\boldsymbol{k}} \times \boldsymbol{g}_s) + (\hat{\boldsymbol{k}} \cdot \boldsymbol{g}_s)(1 - \cos\beta)\hat{\boldsymbol{k}}. \tag{B.3}$$

It is worth noting that because the shear was measured in each galaxy's local (RA, Dec) coordinate frame, the angle of rotation is different for different source galaxies. The transformed shear map $(\widetilde{e_1}, \widetilde{e_2})$ for each galaxy is thus given by

$$\begin{pmatrix} \widetilde{e_1} \\ \widetilde{e_2} \end{pmatrix} = \begin{pmatrix} \cos 2\phi_s & \sin 2\phi_s \\ -\sin 2\phi_s & \cos 2\phi_s \end{pmatrix} \begin{pmatrix} e_1 \\ e_2 \end{pmatrix}, \tag{B.4}$$

where for each source galaxy, the rotation angle ϕ_s is defined by the angular change of its local coordinate frame, for example, the declination to the y-axis of the filament.